NUMERICAL SIMULATIONS OF HIGH SPEED INLET FLOWS

F. Grasso[*] and M. Marini[‡]

Dipartimento di Meccanica e Aeronautica
Università di Roma "La Sapienza", Roma, Italy

Abstract

In this paper a multiblock finite volume technique with a second order total variation diminishing spatial discretization and an efficient implicit time integration has been used to simulate complex internal flows at high Mach numbers. The method employs a lower and upper approximate factorization of the implicit operator with symmetric successive over relaxation sweeps. In the presence of multiblocks a synchronous interface treatment has been devised for an accurate coupling of the blocks. A detailed validation by comparison of the computed results with experiments has shown the capabilities of the method to resolve complex high speed internal flows. A complete analysis of the inlet configurations of a hypersonic vehicle has been performed, evaluating the inlet performances during the phases of acceleration at low altitude and cruise at high altitude.

Introduction

The rapid increase of air traffic all over the world is stimulating the development of hypersonic airbreathing vehicles. The successful development of new transportation systems depends on the propulsion system and its integration with the airframe. When flying at high speed the fluid dynamic performances of the inlet play an important role: the inlet must supply a uniform mass flow, with some prescribed values of pressure, temperature and velocity, to the combustion chamber , and a given value of pressure recovery.

Hypersonic flows through inlets are dominated by complex phenomena and must be optimized over the entire flight envelope. For a realistic simulation, shock-shock, shock-expansion and shock-wave boundary-layer interactions must be accounted for. Strong viscous-inviscid interactions, typical of high Mach number flows, produce substantial modifications of the flow structure: separation and recirculation regions, with upstream propagation of disturbances through the boundary layer, and laminar-turbulent transition. Off-design operation of fixed inlet geometries is physically possible only if flow spillage is allowed.

These phenomena can be correctly predicted only by solving the complete Navier Stokes equations, whose solution requires a strong computational effort in terms of CPU time, storage capacity, etc.. In recent years, several investigators have analyzed the flows through supersonic and hypersonic inlets. Knight [1] made numerical simulations of realistic high speed inlets by solving the Navier Stokes equations and using a flow geometry divided into overlapping regions. Garnero [2] applied the multiblock technique to compute ramjet and scramjet inlet flows; Fujimoto, Niwa and Sawada [3] have simulated the flow through supersonic inlets and the effects of bleed and throat bypass systems, by solving the Navier Stokes equations by means of a finite volume formulation coupled with a second order accurate (MUSCL) scheme.

In the present work, high Mach number inlet flows are analyzed by solving the unsteady Navier Stokes equations. The implicit finite volume multiblock total variation diminishing approach developed in Refs. (5)–(7) has been here applied. The multiblock technique is the most qualified for realistic inlet flow simulations. The multiblock approach consists in partitioning the computational domain into regions, called blocks, so that: 1) the topology of each block is rather simple; 2) the grid for each block can be easily generated. The partitioning of the computational domain in blocks introduces interfaces. The treatment of such interfaces plays a critical role, especially in the presence of discontinuities that cross the interfaces. To inhibit spurious oscillations and distortion of shocks, and to ensure conservation, information between adjacent blocks must be properly exchanged. A synchronous approach has been developed, whereby each block is computed sequentially with an implicit interface treatment.

Hypersonic inlet flows have been computed to test the validity of the implicit finite volume multiblock approach. The computed results are compared with available experimental data, and show that the method is well suited to predict complex internal flows.

Governing Equations

The governing equations solved are the compressible unsteady Navier Stokes equations in conservation form:

$$\frac{d}{dt} \int_S \mathbf{W} \, dS = - \oint_{\partial S} (\mathbf{F}_E - \mathbf{F}_V) \cdot \mathbf{n} \, ds \qquad (1)$$

where $\mathbf{W}$, $\mathbf{F}_E$ and $\mathbf{F}_V$ are, respectively, the vector unknown, the inviscid and viscous fluxes, defined as:

---

[*]Associate Professor, Member AIAA
[‡]Ph.D Student

$$\mathbf{W} = [\rho, \rho\mathbf{u}, \rho E]^T \tag{2}$$

$$\mathbf{F}_E = [\rho\mathbf{u}, \rho\mathbf{uu} + p\mathbf{I}, \rho\mathbf{u}\,(E + p/\rho)]^T \tag{3}$$

$$\mathbf{F}_V = [0, \underline{\sigma}, -\left(\mathbf{q} - \mathbf{u} \cdot \underline{\sigma}\right)]^T \tag{4}$$

and

$$\underline{\sigma} = \mu\left(\nabla\mathbf{u} + \nabla\mathbf{u}^T\right) - \frac{2}{3}\mu\nabla\cdot\mathbf{u}\,\mathbf{I} \tag{5}$$

$$\mathbf{q} = -\gamma\,\frac{\mu}{Pr}\,\nabla e \tag{6}$$

$$\mu - \mu_t = \begin{cases} \mu_\infty\,\widetilde{T} & \text{if } \widetilde{T} \le s_1 \\[2ex] \mu_\infty\,(s_1\,\widetilde{T})^{1/2}\,\dfrac{1 + s_2/s_1}{1 + s_2\big/\widetilde{T}} & \text{if } \widetilde{T} > s_1 \end{cases} \tag{7}$$

where $\widetilde{T} = T/T_\infty$; $s_1 = 120/T_\infty$; $s_2 = 110/T_\infty$.
The turbulent viscosity μ_t is defined according to the algebraic turbulence model of Baldwin and Lomax.[4]

Numerical Solution

Realistic inlets are geometrically complex to allow proper compression of the flow. Moreover, the design of the inlets is such that the compression may be of a mixed type, both external and internal. Consequently, for an accurate modeling of the flow one must account for spillage, bleeding (necessary to have off-design operations with a fixed inlet geometry) and proper treatment of complex geometries. Hence, a solver for simulating flows through inlets should have either block or unstructured capabilities.

At the present stage, the performance of block structured approaches is better than the unstructured ones, also on account of the fact that the former can be easily parallelized. For this reason, in the present work a multiblock approach has been employed together with a high resolution implicit scheme.

For two-dimensional inlet flow simulations, the use of only two blocks is sufficient to account for spillage. For each block the computational grid is generated independently. The two meshes are equally spaced in the x direction, and highly stretched in the y direction. In particular, for an accurate resolution of the shock-wave boundary-layer interaction, the near wall cells must have mesh spacing $\Delta y = o(10^{-4})$ and an aspect ratio $\Delta x/\Delta y = o(10^2)$, as shown in Ref. (5).

Finite Volume Formulation

Space and time discretizations are separated by using the method of lines, and a system of ordinary differential equations is obtained for every computational cell. A cell centered finite volume formulation is employed and, approximating surface and boundary integrals by means of the mean value theorem and mid-point rule, the governing equations are cast in the following discretized form [5]:

$$S_{i,j}\,\frac{d\mathbf{W}_{i,j}}{dt} + \sum_{\beta=1}^{4}(\mathbf{F}_{num}\cdot\mathbf{n}\Delta s)_\beta = 0 \tag{8}$$

where β stands for the generic cell face, $\mathbf{n}$ is the positive unit normal to cell face whose length is Δs, and $S_{i,j}$ is the cell area.

The numerical flux vector is:

$$\mathbf{F}_{num} = \mathbf{F}_{E,num} - \mathbf{F}_{V,num} \tag{9}$$

Numerical inviscid flux discretization

An upwind biased second order TVD scheme has been used to evaluate the inviscid flux contribution. The scheme has good properties of monotonicity and conservativity in the presence of discontinuities, and it yields second order accuracy and oscillation free solutions (strictly true for a one-dimensional scalar equation). Thus, enforcing consistency at cell face $i + 1/2, j$, one has:

$$(\mathbf{F}_{E,num}\cdot\mathbf{n}\Delta s)_{i+1/2,j} = \\ \left[\frac{1}{2}(\mathbf{F}_{E_{i,j}} + \mathbf{F}_{E_{i+1,j}})\cdot\mathbf{n} + \mathbf{\Phi}_{i+1/2,j}\right]\Delta s_{i+1/2,j} \tag{10}$$

The term $\mathbf{\Phi}_{i+1/2,j}$ represents the numerical antidiffusive flux contribution, that modifies the inviscid flux to make the scheme upwind biased TVD and second order accurate. Its expression is obtained by characteristic decomposition in the direction normal to cell face, thus obtaining [8,9]:

$$\mathbf{\Phi}_{i+1/2} = \frac{1}{2}\sum_{k=1}^{4}[\psi(a_{i+1/2}^k)\,(g_i^k + g_{i+1}^k) - \\ \psi(a_{i+1/2}^k + \gamma_{i+1/2}^k)\alpha_{i+1/2}^k]\mathbf{R}_{i+1/2}^k \tag{11}$$

where the subscript j has been dropped for simplicity, and $\mathbf{R}_{i+1/2}^k$ is the $k-th$ eigenvector. The right eigenvector matrix of the normal inviscid flux jacobian is defined [10] in terms of the normal (U) and tangential (V) velocity components, as given in the following

$$\mathbf{R}_{i+1/2} = \begin{pmatrix} 1 & 1 & 1 & 0 \\[1.5ex] u - \cos\theta & u & u + \cos\theta & -\sin\theta \\[1.5ex] v - \sin\theta & v & v + \sin\theta & \cos\theta \\[1.5ex] H - Uc & \frac{u^2+v^2}{2} & H + Uc & V \end{pmatrix}_{i+1/2}$$

where $\cos\theta$, $\sin\theta$ are the components of the unit normal, and Roe's averaging is used to evaluate u, v, c, H at $i + 1/2$.

The vector $\underline{\alpha}_{i+1/2}$ is the difference of the characteristic variables, defined as:

$$\underline{\alpha}_{i+1/2} = \mathbf{R}_{i+1/2}^{-1}\Delta_{i+1/2}\mathbf{W} \tag{12}$$

The entropy function ψ here adopted is that of Harten [8]:

$$\psi(z) = \begin{cases} \dfrac{1}{2}\left(\dfrac{z^2}{\delta} + \delta\right) & if \quad z < \delta \\[2ex] |z| & if \quad z \ge \delta \end{cases} \tag{13}$$

where δ is a parameter that enforces the entropy condition for vanishing eigenvalues, whose value depends on the type

of flow to be computed. For all cases a value of $\delta = 0.425$ has been used.

A minmod flux limiter is employed for the antidiffusive flux g:

$$g_i^k = minmod\ (\alpha_{i-1/2}^k, \alpha_{i+1/2}^k) \qquad (14)$$

The characteristic speed γ^k of the antidiffusive flux is given by:

$$\gamma_{i+1/2}^k = \psi(a_{i+1/2}^k) \begin{cases} \dfrac{g_{i+1}^k - g_i^k}{\alpha_{i+1/2}^k} & if \quad \alpha_{i+1/2}^k \neq 0 \\ \\ 0 & if \quad \alpha_{i+1/2}^k = 0 \end{cases} \qquad (15)$$

For second order accuracy, boundary conditions on g are required. At all boundaries the normal derivative of g has been set equal to zero. Conservation is enforced by imposing that, for all cells along the walls, the contribution (due to the modified flux $\boldsymbol{\Phi}$) in the direction normal to the wall is zero.

Numerical viscous flux discretization

According to the constitutive equations, the viscous fluxes depend upon the gradients of the unknown vector, and the numerical counterpart is obtained by applying Gauss theorem to a computational cell whose vertices are the two grid nodes (I, J) and $(I, J-1)$ and the centers of the two adjacent cells (i, j) and $(i+1, j)$. For an arbitrary function φ the numerical derivatives at $i+1/2, j$ are evaluated according to the following formulas:

$$\left(\frac{\partial \varphi}{\partial x}\right)_{i+1/2,j} = \frac{\Delta_i \varphi \, \Delta_j y - \Delta_j \varphi \Delta_i y}{\Delta_i x \, \Delta_j y - \Delta_j x \, \Delta_i y}$$

$$\left(\frac{\partial \varphi}{\partial y}\right)_{i+1/2,j} = -\frac{\Delta_i \varphi \, \Delta_j x - \Delta_j \varphi \, \Delta_i x}{\Delta_i x \, \Delta_j y - \Delta_j x \, \Delta_i y}$$

where

$$\Delta_i(.) = (.)_{i+1,j} - (.)_{i,j} \quad ; \quad \Delta_j(.) = (.)_{I,J} - (.)_{I,J-1}$$

The grid values $\varphi_{I,J}$, $\varphi_{I,J-1}$ are obtained by bilinear interpolation of cell center values. Hence, the discretized viscous flux contribution at cell face $i+1/2, j$ is an algebraic function of grid and cell center values, i.e.

$$(\mathbf{F}_{V,num})_{i+1/2,j} = f\ (\mathbf{W}_{i,j}; \mathbf{W}_{i+1,j}; \mathbf{W}_{I,J}; \mathbf{W}_{I,J-1}) \qquad (16)$$

Implicit Solver

Linearization of the flux vectors about the previous time step yields the unfactored implicit form of the equations [5,6]:

$$S_{i,j} \frac{\Delta \mathbf{W}_{i,j}}{\Delta t} + \eta \sum_{\beta=1,3} [(\mathbf{A} + \mathbf{P})\Delta s \Delta \mathbf{W}]_\beta +$$

$$\eta \sum_{\beta=2,4} [(\mathbf{B} + \mathbf{Q})\Delta s \Delta \mathbf{W}]_\beta = \mathbf{R}_{i,j}^n \qquad (17)$$

where $\mathbf{R}_{i,j}^n$ is the residual; $\Delta \mathbf{W}_\beta$ is the time variation of the solution at cell face β; and η is a weighting factor, that weighs the numerical flux between the time levels n and $n+1$. The matrices $\mathbf{A}$ ($\mathbf{B}$) and $\mathbf{P}$ ($\mathbf{Q}$) are the jacobians of the inviscid and viscous fluxes in the direction normal to cell faces $i \pm 1/2, j$ ($i, j \pm 1/2$):

$$\mathbf{A} = \frac{\partial}{\partial \mathbf{W}}(\mathbf{F}_E \cdot \mathbf{n})_{i\pm1/2,j} \quad ; \quad \mathbf{P} = \frac{\partial}{\partial \mathbf{W}}(\mathbf{F}_V \cdot \mathbf{n})_{i\pm1/2,j}$$

A block triangular form of the implicit operator is obtained as follows. First, using flux difference concepts, the contribution of the inviscid flux jacobians at each cell face is split into the positive and negative part. The positive (negative) inviscid flux jacobian matrix $\mathbf{A}^+$ ($\mathbf{A}^-$) is constructed so that it has non negative (non positive) eigenvalues. To obtain a well conditioned diagonally dominant operator matrix, the following formulas [5,6] have been used

$$\mathbf{A}^\pm = \omega^e \frac{\mathbf{A} \pm \rho_A \mathbf{I}}{2} \qquad (18)$$

$$\rho_A = r_A \max(|\lambda(\mathbf{A})|) \qquad (19)$$

where $\lambda(\mathbf{A})$ are the eigenvalues of the inviscid flux jacobian, r_A is a constant of $o(1)$ that affects the stability and convergence, ω^e is a relaxation parameter that enhances the effects of the inviscid eigenvalues (a value of ω^e equal to 2 has been used), and $\mathbf{I}$ is the unit matrix. Then, at cell face $i+1/2, j$ one has

$$(\mathbf{A} \Delta \mathbf{W})_{i+1/2,j} = \mathbf{A}_{i,j}^+ \Delta \mathbf{W}_{i,j} + \mathbf{A}_{i+1,j}^- \Delta \mathbf{W}_{i+1,j} \qquad (20)$$

The viscous flux jacobians are reduced to a diagonal form by using the spectral radii,[5,6] thus obtaining:

$$\mathbf{P} = \omega^v\ k_x n_x \mathbf{I} \qquad (21)$$

where k_x is the spectral radius of the viscous jacobian matrix and ω^v is a relaxation parameter introduced to inhibit the effects of the viscous eigenvalues (a value of ω^v equal to $1/2$ has been used). The matrices $\mathbf{B}$ and $\mathbf{Q}$ are similarly defined.

To reduce the computational effort a symmetric successive over relaxation technique is implemented,[5,6] thus eliminating the need for 4×4 matrix inversion at each cell. Substituting Eqs. (18)–(21) and neglecting the variations of Δs_β in the x and y directions (strictly valid only for undistorted cells), the following scalar diagonal matrix is obtained

$$\mathbf{N} = [1 + \alpha(\rho_A \Delta s_{1,3} + \rho_B \Delta s_{2,4})]\mathbf{I} \qquad (22)$$

where

$$\alpha = \eta(\Delta t/S)_{i,j} \quad ; \quad \Delta s_{\ell,m} = \frac{\Delta s_\ell + \Delta s_m}{2}$$

Then, Eq. (17) is reduced to the following factorized form:

$$\mathbf{L} \cdot \mathbf{U} \Delta \mathbf{W}_{i,j} = \beta\, \mathbf{N}\, \mathbf{R}_{i,j} \qquad (23)$$

where $\beta = (\Delta t/S)_{i,j}$, and $\mathbf{L}$, $\mathbf{U}$ are the lower and upper factors. For steady state solutions, the efficiency of the method has been improved by freezing the evaluation of the jacobian matrices for $o(m)$ cycles. Numerical experiments [5,6] indicate that the higher the Mach number is, the more often the jacobian matrices need to be evaluated: for supersonic flows m is $o(10)$; for hypersonic flows m is $o(2)$. The solution of Eq. (23) is obtained in three phases:

Forward Sweep

Once the residual $\mathbf{R}_{i,j}$ is calculated at time level n, the forward sweep is performed:

$$\mathbf{L}\,\Delta\,\mathbf{W}_{i,j}^* = \beta\,\mathbf{N}\,\mathbf{R}_{i,j}^n \qquad (24)$$

Eq. (24) is inverted performing a cell by cell sweep in the forward direction, starting from the bottom left-most corner, thus yielding at each cell i,j:

$$\Delta\mathbf{W}_{i,j}^* = \mathbf{N}^{-1}\,(\mathbf{N}\mathbf{R}_{i,j}^n + \\ \alpha\mathbf{A}_{i-1,j}^+\Delta s_3\Delta\mathbf{W}_{i-1,j}^* + \alpha\mathbf{B}_{i,j-1}^+\Delta s_4\Delta\mathbf{W}_{i,j-1}^*) \quad (25)$$

At the left and bottom boundaries $\Delta\mathbf{W}^*$ is set equal to zero.

Backward Sweep

Once $\Delta\mathbf{W}_{i,j}^*$ is obtained, the domain is swept in the backward direction (starting from the top right-most corner) and the time change of the solution is obtained according to the following equation:

$$\mathbf{U}\,\Delta\,\mathbf{W}_{i,j} = \Delta\,\mathbf{W}_{i,j}^* \qquad (26)$$

By matrix inversion of Eq. (26) one has

$$\Delta\mathbf{W}_{i,j} = \mathbf{N}^{-1}\,(\mathbf{W}_{i,j}^* - \\ \alpha\mathbf{A}_{i+1,j}^-\Delta s_1\Delta\mathbf{W}_{i+1,j} - \alpha\mathbf{B}_{i,j+1}^-\Delta s_2\Delta\mathbf{W}_{i,j+1}) \quad (27)$$

At the top and right boundaries $\Delta\mathbf{W}$ is set equal to zero.

Updating of the Solution

Once $\Delta\mathbf{W}_{i,j}$ is computed, the solution is updated as follows:

$$\mathbf{W}_{i,j}^{n+1} = \mathbf{W}_{i,j}^n + \Delta\mathbf{W}_{i,j} \qquad (28)$$

Multiblock technique

The multiblock strategy here devised uses patched blocks. However, for an efficient treatment of the boundary conditions, fictitious cells are introduced along the boundaries, and the blocks are effectively overlaid. To properly couple the blocks at the interfaces, the continuity of the variables is imposed by injecting the solution of the underlaying block onto the overlaying one [7] (see Fig. 1).

For the block interface treatment a synchronous approach has been employed, that consists to solve sequentially the two blocks. Referring to Fig. 2, the solution of block 1 is computed first (phases L.1 and U.1). Then, the solution is injected onto block 2 at the interface (phase I.12). Finally, block 2 is updated by performing the two sweeps (phases L.2 and U.2), and the auxiliary cells of block 1 are updated by injecting the block 2 solution (phase I.21). Referring to Fig. 2, to start the forward sweep on block 2, the block matrix $\mathbf{B}_{i,1}^+$ of Eq. (25), is required. Likewise, to start the backward sweep on block 1, the block matrix $\mathbf{B}_{i,nj+1}^-$ of Eq. (27) is needed. According to the interface treatment, these two matrices are function of variables exchanged between the blocks and are determined as:

$$(\mathbf{B}_{i,1}^+)_{block\,2} = (\mathbf{B}_{i,nj}^+)_{block\,1} \qquad (phase\ I.12) \qquad (29)$$

$$(\mathbf{B}_{i,nj+1}^-)_{block\,1} = (\mathbf{B}_{i,2}^-)_{block\,2} \qquad (phase\ I.21) \qquad (30)$$

Results

A complete study of the inlet behaviour of an airbreathing hypersonic vehicle has been performed to assess the validity of the present finite volume multiblock approach. Two different flight conditions have been analyzed corresponding to the acceleration at low altitude and cruise at high altitude.

Two geometric configurations, differing in the internal compression ratio β_c (defined as the ratio of throat pressure to entrance pressure), have been studied. They correspond to the NASA P2 and NASA P8 inlets,[11] where the number stands for the design value of internal compression ratio, that have been designed to achieve high efficiency and approximately uniform static pressure at throat section. The choice of the internal compression ratio depends on the mission requirements: the lowest value (yielding a throat pressure ratio $(p/p_\infty)_{th} = 6.25$) corresponds to the acceleration phase at low altitude, while the highest value (that give $(p/p_\infty)_{th} = 25.0$) is representative of the cruise at high altitude.

Experimental tests have been conducted in the NASA Ames 3.5-Foot Hypersonic Wind Tunnel [11] at a nominal freestream Mach number $M_\infty = 7.4$ and unit Reynolds number $Re_\infty = 8.86 \times 10^6\,m^{-1}$. The freestream total pressure and temperature are, respectively, $p_\infty^0 = 4.14 \times 10^6$ Pa and $T_\infty^0 = 811$ K, and the wall temperature is $T_{wall} = 303$ K. In the experimental apparatus a forebody wedge of $\theta = 6.5$ deg was used to yield at the inlet entrance section a design Mach number of about 6.0, which corresponds to a vehicle flying at Mach number $M = 12$. The throat height (h_{th}) varies from about 2 to 6 cm. and the contraction ratio (CR), defined as the ratio of the ideal capture area to the throat area, varies between 3 and 7.7 (see Table 1). In the Table 1 the values of throat location X_{th} and throat height h_{th} are expressed in cm. . For all computations real gas effects have been neglected, due to the rather low temperature values, and the flow is assumed to be fully turbulent.

NASA P2 inlet

The NASA P2 inlet represents a typical configuration for the acceleration at low altitude, with low contraction ratio ($CR = 3.007$) and low internal compression ratio ($\beta_c = 2$). This inlet configuration is such that the cowl generated shock wave should cancel at the centerbody, to provide a uniform flow at the throat. The numerical solution has been obtained by using two blocks of 176×48 and 176×14 cells, with the normal mesh spacing Δy ranging from $0.5 \cdot 10^{-3}$ to $0.5 \cdot 10^{-1}$, with an aspect ratio of about 90 in the proximity of the wall. Approximately 20 cells (at the throat section) are fitted within the centerbody boundary layer, and about 15 cells within the cowl boundary layer. The computation has been performed with a CFL number equal to 2, the jacobian matrices have been reevaluated every 2 cycles, and the parameters r_A, r_B, which affect the diagonal dominance of the implicit operator, have been set equal to 1.6.

Iso-pressure contour lines are shown in Fig. 3. The shock wave that is generated at the wedge leading edge crosses the interface between the two blocks ahead of the cowl leading edge, thus allowing for flow spillage. The shock wave generated at the cowl lip reflects on the centerbody and interacts weakly with the boundary layer and with the expansion waves generated toward the exit section. Thus, on the internal cowl surface the flow is practically undisturbed almost everywhere, with a little pressure drop due to the expansion upstream of the exit section. The centerbody and cowl pressure p/p_∞ vs x/L (where L is the height of the inlet entrance section) are plotted in Figs. 4, 5. The pressure levels are slightly higher than the experimental and design values [11] (about 13% at throat section, both for centerbody and cowl), and this is mainly due to the absence of three-dimensional effects and most likely to the simple algebraic turbulence model here employed. However, the cowl shock impingement position on the centerbody is well predicted. The pressure along the cowl is constant, in agreement with the experimental and design values. The predicted internal compression ratio agrees well with the design value ($\beta_c = 2.027$, difference of 1%), while the average static pressure at the throat section is only slightly over-predicted (the difference is about 3%).

Detailed comparisons of the computed and measured [11] flow properties at the inlet entrance section ($x = 81.28$ cm.) are shown in Figs. 6–8. The static pressure, Mach number and total temperature distributions agree well with the experiments. The thickness of the boundary layer is also well predicted. Some discrepancies are found in the total pressure recovery distribution (not reported). However, the effects of the cowl lip shock and flow spillage on the accuracy of the measurements are not indicated. At the throat station ($x = 119.38$ cm.) flow uniformity is achieved as shown in Figs. 9–11, where the static pressure, the Mach number and total pressure distributions are reported. The Mach number of the core flow is well predicted (about 5) and the relatively thick boundary layer is clearly observed. The predicted static pressure is about 13% higher than the experimental one and a rapid decrease of pressure is observed on the edge of centerbody boundary layer, probably due to the mechanism of shock-wave boundary-layer interaction.

NASA P8 inlet

The NASA P8 inlet represents the configuration for hypersonic airbreathing vehicle cruise, with high contraction ratio ($CR = 7.7$) and is designed to provide an internal throat compression ratio $\beta_c = 8$. The geometric configurations of the two inlets are the same up to $x = 87.0$ cm. . Then, the NASA P8 centerbody and cowl profiles are designed in such a way that the resulting thrust of the propulsive module is aligned with the longitudinal axis of the vehicle, which is a desiderable condition to maximize the propulsive efficiency in cruise operation.

The computation has been performed by using two blocks with the same number of cells as in the previous case, normal mesh spacing varying between $0.2\cdot10^{-3}$ and $0.5\cdot10^{-1}$ and the aspect ratio near the wall is about 240. About 20 cells are fitted within both the centerbody and cowl boundary layers at the throat section. The computation has been performed with the same numerical parameters used in the previous test case.

Compression waves are generated by the continous curvature of the internal cowl surface and are clearly shown in the iso-pressure contours of Fig. 12. The centerbody and cowl pressure distributions p/p_∞ vs x/L are shown in Figs. 13, 14. Having neglected the three-dimensional effects, the pressure level is over-predicted with respect to the experiments [11] (about 20% on the centerbody and 11% on the cowl, both at throat section). Along the cowl the numerical solution is in good agreement with the experiments. The design pressure value is constant in the region of the throat, and the cowl shock only partially cancels at the centerbody. The computed internal compression ratio is equal to $\beta_c = 9.957$, in disagreement with the design value of 8; however it is in better agreement with the (estimated) measured value $\beta_c = 8.611$. The disagreement with respect to the design is due to the fact that the cowl generated shock wave does not cancel at centerbody, but reflects strongly and affects the flow approaching the throat region. Moreover, the interaction between the cowl generated shock wave and the centerbody boundary layer causes a nearly separated flow.

Figures 15–17 show the static pressure, the Mach number and total temperature distributions at the throat section ($x = 125.73$ cm.). The predicted static pressure is slightly higher than the experimental one (again due to the absence of three dimensional effects). However, in the proximity of the centerbody a pressure value close to the design one is predicted. Very good agreement is shown for the Mach number and total temperature.

Overall Performances

The predicted overall performances of the two inlets are reported in Table 1, expressed in terms of the pressure recovery factor (η_p) and the kinetic efficiency (η_k), defined as [12]

$$\eta_p = \frac{p^0_{exit}}{p^0_\infty}$$

$$\eta_k = 1 - \frac{2}{(\gamma - 1)M_\infty^2}\left[\left(\frac{p^0_\infty}{p^0_{exit}}\right)^{\frac{\gamma-1}{\gamma}} - 1\right]$$

As the contraction ratio increases, the shock waves become stronger and yield greater total pressure losses. As a consequence, the pressure recovery factor and the kinetic efficiency decrease. However, the former is affected the most. The predicted values are reported in Table 1. Observe that for the highest compression ratio configuration the shock-wave boundary-layer interaction is more critical, and it yields a nearly separated flow, thus giving an even lower pressure recovery factor.

Conclusions

A multiblock finite volume technique with a total variation diminishing scheme and an implicit time algorithm has been applied to compute high Mach number inlet flows. The blocks are accurately coupled by means of a synchronous in-

terface treatment. A detailed analysis of the inlet behaviour of an airbreathing hypersonic vehicle has been performed, evaluating the overall performances of the inlet in two flight conditions: acceleration at low altitude and cruise at high altitude.

Comparisons with experimental results have shown that the technique has good capabilities to compute complex high speed internal flows. The static pressure, Mach number and total temperature distributions are well predicted. The wall pressure levels are over-predicted, mainly due to the absence of three-dimensional effects, the fully turbulent assumption and the intrinsic limitations of the algebraic turbulence model employed. However, the model is capable of predicting the effects of the contraction ratio and shockwave boundary-layer interaction on the inlet performances.

References

[1] Knight D.D.,"Numerical Simulation of Realistic High-Speed Inlets Using the Navier-Stokes Equations", *AIAA Journal*, Vol. 15, 1977, pp. 1583–1589.

[2] Garnero P., "Ramjet Applications at Aérospatiale", *The third joint Europe/US short course in hypersonics*, 1990.

[3] Fujimoto A., Niwa N. and Sawada K., "Numerical Investigation on Supersonic Inlet with Realistic Bleed and Bypass Systems", AIAA paper 91-0127, 1991.

[4] Baldwin B.S., Lomax H., "Thin Layer Approximation and Algebraic Model for Separated Turbulent Flows", AIAA paper 78-0257, 1978.

[5] Grasso F., Marini M., "LU Implicit TVD Scheme for the Solution of Viscous Two Dimensional High Speed Flows", *AIAA 10th CFD Conference*, 1991, pp. 518–528.

[6] Grasso F., Marini M., "LU Implicit TVD Scheme for the Solution of Viscous High Speed Flows", to appear in *AIAA Journal*, Vol. 30, August 1992.

[7] Grasso F., Marini M., "Multiblock Implicit TVD Solution of High Speed Internal Flows", submitted to *Journal of Propulsion and Power*, 1992.

[8] Yee H.C., Warming R.F. and Harten A., "Implicit TVD Schemes for Steady State Calculations", *Journal of Computational Physics*, Vol. 57, 1985, pp. 327–360.

[9] Yee H.C., Klopfer G.H. and Montagnè J.L., "High Resolution Shock Capturing Schemes for Inviscid and Viscous Hypersonic Flows", NASA TM 100097, 1988.

[10] Bassi F., Grasso F. and Savini M., "Finite Volume TVD Runge-Kutta Scheme for Navier Stokes Computations", *Lecture Notes in Physics*, Springer Verlag, Vol. 323, 1989, pp. 131-136.

[11] Gnos A.V., Watson E.C., Seebaugh W.R., Sanator R.J. and DeCarlo J.P., "Investigation of Flow Fields within Large-Scale Hypersonic Inlet Models", NASA TN D-7150, 1973.

[12] Billig F.S., "Ramjets with Supersonic Combustion", AGARD LS 136, 1984.

Table 1 – Inlet Performances

Model	X_{th}	h_{th}	CR	β_c	η_p	η_k
P2	119.38	6.091	3.007	2.027	0.493	0.979
P8	125.73	2.377	7.707	9.957	0.356	0.968

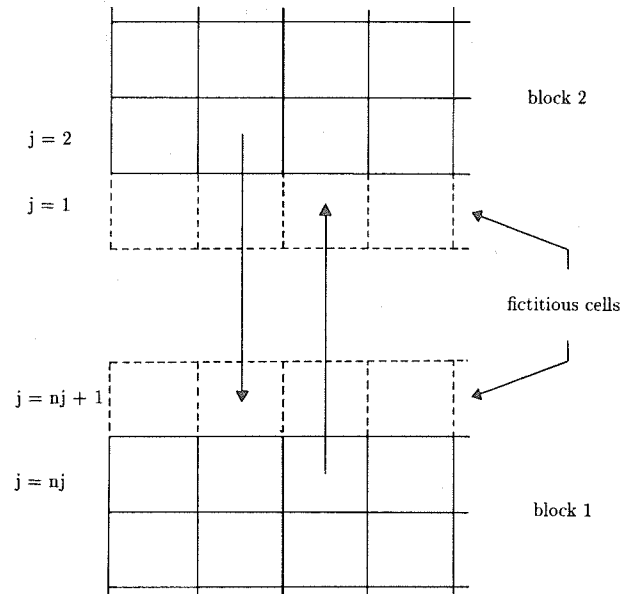

Fig. 1 Block interface treatment
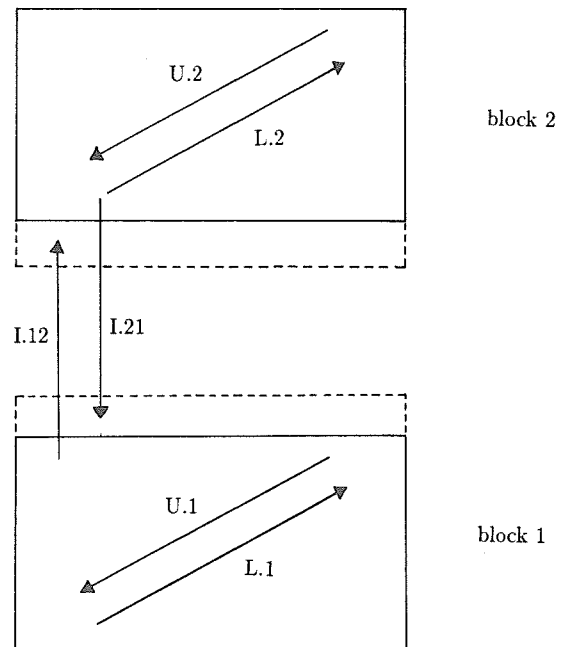

Fig. 2 Schematic of synchronous interface treatment

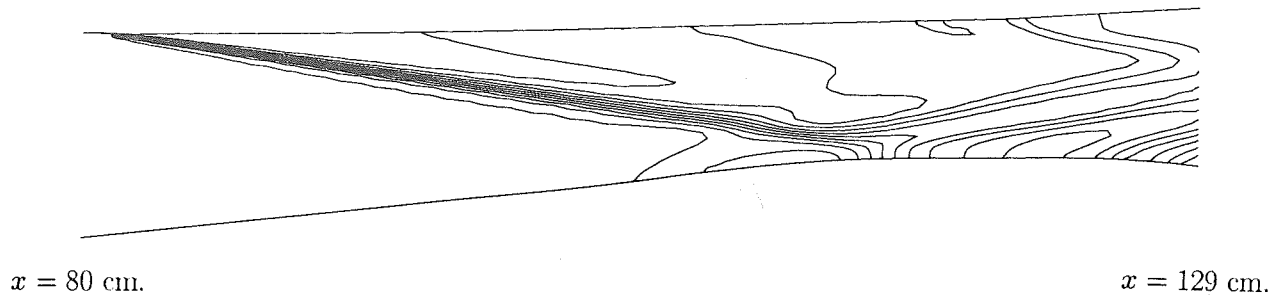$x = 80$ cm. $x = 129$ cm.

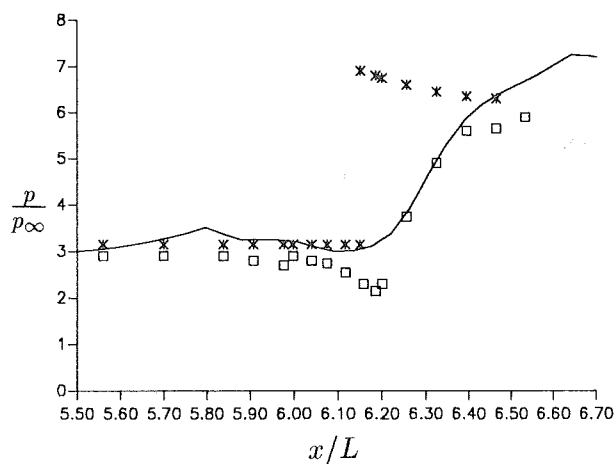Fig. 3 Iso-pressure lines (Δp=0.50) for NASA P2 hypersonic inlet

Fig. 4 Centerbody pressure p/p_∞ vs x/L for NASA P2 hypersonic inlet (—, computed; □, experimental [11]; *, design [11])
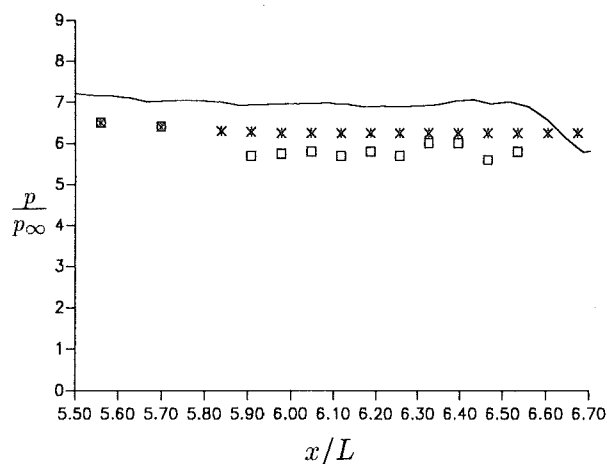

Fig. 5 Cowl pressure p/p_∞ vs x/L for NASA P2 hypersonic inlet (—, computed; □, experimental [11]; *, design [11])
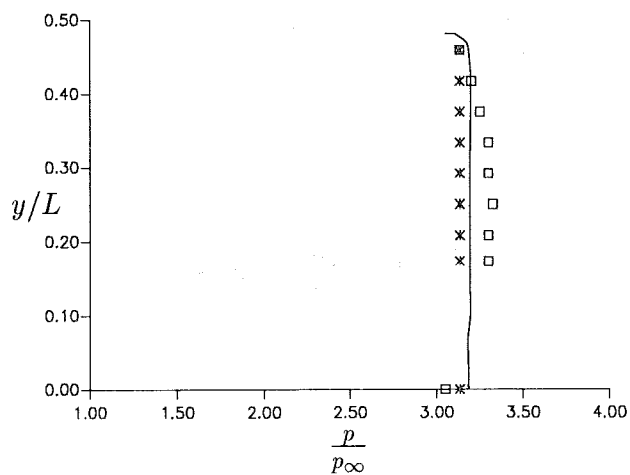

Fig. 6 Static pressure profile at inlet entrance section (—, computed; □, experimental [11]; *, design [11])
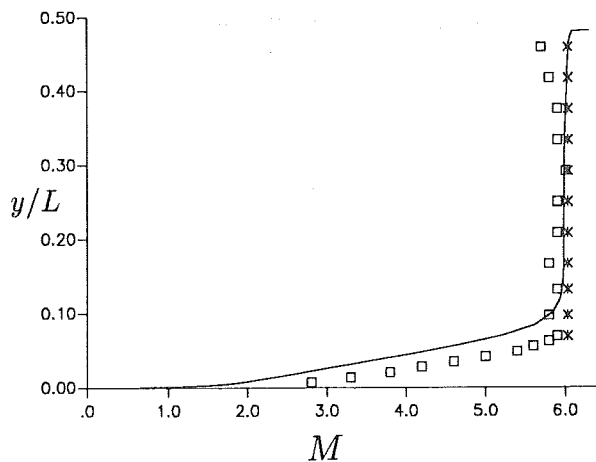
Fig. 7 Mach number profile at inlet entrance section (—, computed; □, experimental [11]; *, design [11])

734
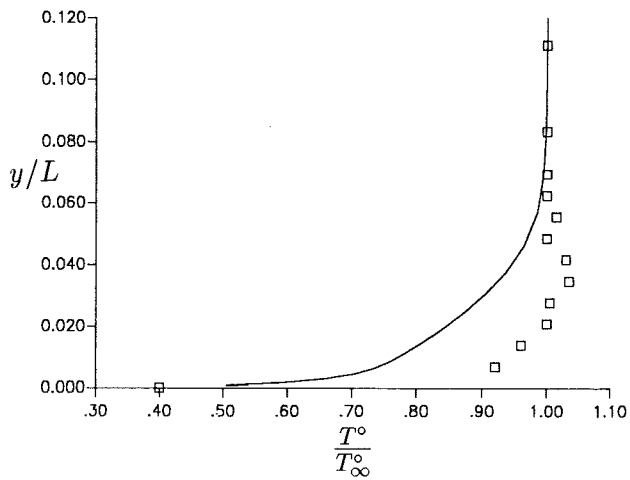
Fig. 8 Total temperature profile at inlet entrance section (—, computed; □, experimental [11])
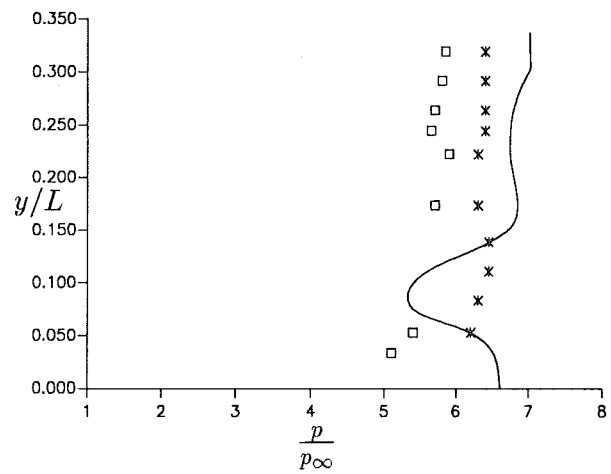
Fig. 9 Static pressure profile at NASA P2 throat section (—, computed; □, experimental [11]; *, design [11])
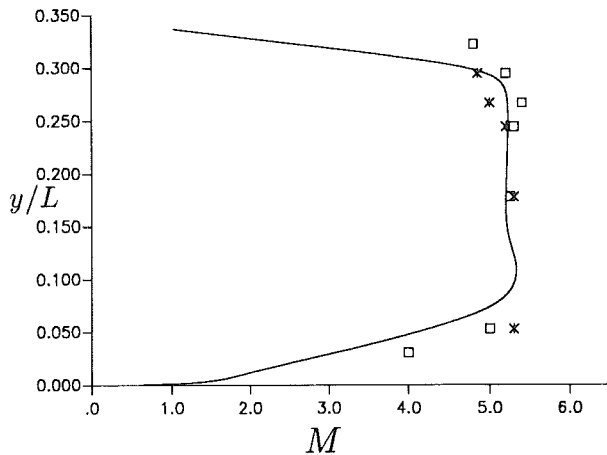
Fig. 10 Mach number profile at NASA P2 throat section (—, computed; □, experimental [11]; *, design [11])
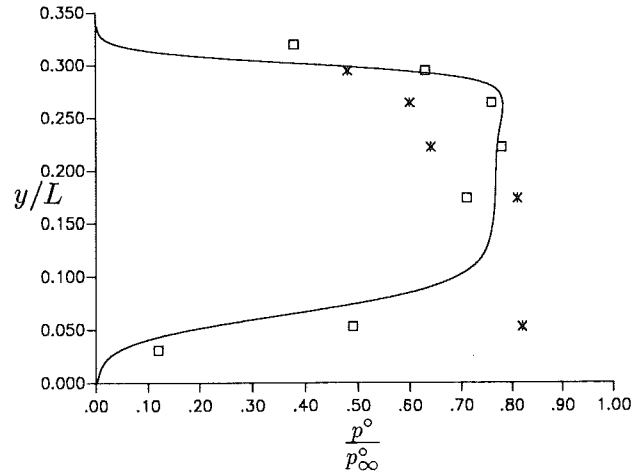
Fig. 11 Total pressure recovery profile at NASA P2 throat section (—, computed; □, experimental [11]; *, design [11])
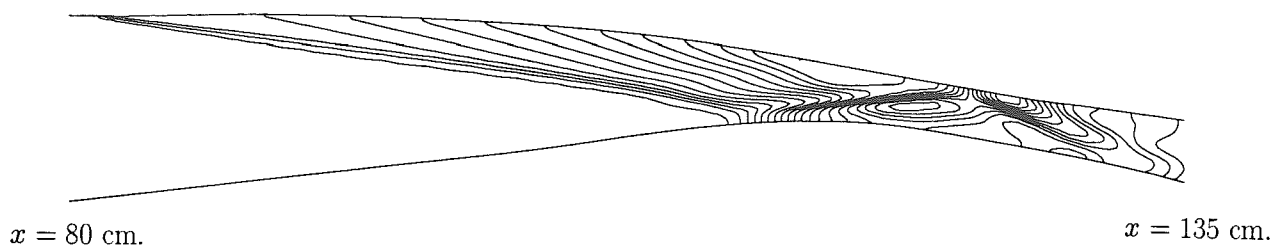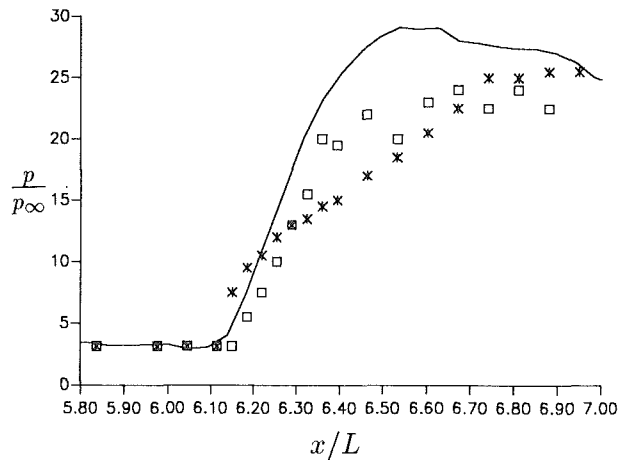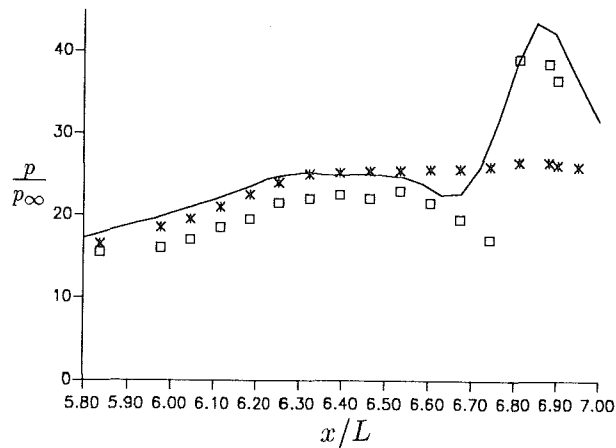
$x = 80$ cm.

$x = 135$ cm.

Fig. 12 Iso-pressure lines ($\Delta p = 1.75$) for NASA P8 hypersonic inlet

Fig. 13 Centerbody pressure p/p_∞ vs x/L for NASA P8 hypersonic inlet (—, computed; □, experimental [11]; *, design [11])

Fig. 14 Cowl pressure p/p_∞ vs x/L for NASA P8 hypersonic inlet (—, computed; □, experimental [11]; *, design [11])
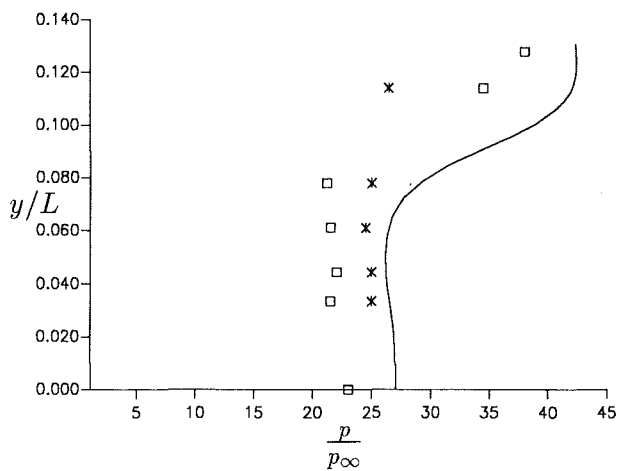

Fig. 15 Static pressure profile at NASA P8 throat section (—, computed; □, experimental [11]; *, design [11])
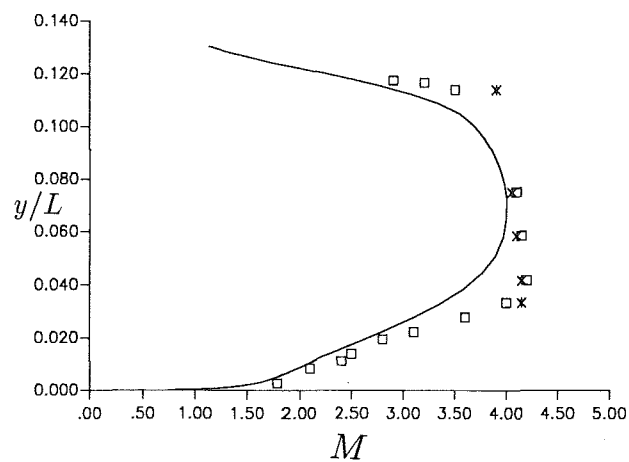

Fig. 16 Mach number profile at NASA P8 throat section (—, computed; □, experimental [11]; *, design [11])
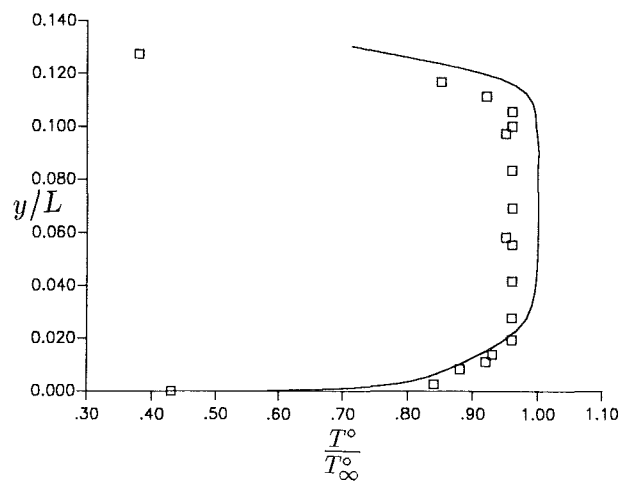

Fig. 17 Total temperature profile at NASA P8 throat section (—, computed; □, experimental [11])